Research Article

Xiangning Zhou, Muhammad Amer Qureshi, Nargis Khan, Wasim Jamshed*,
Siti Suzilliana Putri Mohamed Isa, Nanthini Balakrishnan, and Syed M. Hussain

Thermosolutal Marangoni convective flow of MHD tangent hyperbolic hybrid nanofluids with elastic deformation and heat source

Abstract: In this work, the Marangoni convective flow of magnetohydrodynamic tangent hyperbolic ($Fe_3O_4 - Cu$/ethylene glycol) hybrid nanofluids over a plate dipped in a permeable material with heat absorption/generation, heat radiation, elastic deformation and viscous dissipation is discussed. The impact of activation energy is also examined. Hybrid nanofluids are regarded as advanced nanofluids due to the thermal characteristics and emerging advantages that support the desire to augment the rate of heat transmission. The generalized Cattaneo–Christov theory, which takes into account the significance of relaxation times, is modified for the phenomena of mass and heat transfer. The fundamental governing partial differential equations are converted to ordinary differential equations (ODEs) by adopting similarity variables. The Runge–Kutta–Fehlberg-45 technique is utilized to solve nonlinear ODEs. Regarding the non-dimensional embedded parameters, a graphic investigation of the thermal field, concentration distribution, and velocity profile is performed. The results show that the increasing Marangoni ratio parameter enhances velocity and concentration distributions while decreases the temperature distribution. The velocity profile is decreased and the efficiency of heat transfer is improved as the porosity parameter is increased. Nusselt number is diminished with the rising values of the porosity variable.

Keywords: elastic deformation, tangent hyperbolic hybrid nanofluids, Cattaneo-Christov model, activation energy, Marangoni convection

* **Corresponding author: Wasim Jamshed,** Department of Mathematics, Capital University of Science and Technology (CUST), Islamabad, 44000, Pakistan; Mathematics in Applied Sciences and Engineering Research Group, Scientific Research Center, Al-Ayen University, Nasiriyah 64001, Iraq; Department of Computer Engineering, Biruni University, Topkapi, Istanbul, Turkey, e-mail: wasiktk@hotmail.com
Xiangning Zhou: School of Computer Science and Technology, Shandong Technology and Business University, Yantai 264005, China
Muhammad Amer Qureshi: PYP-Mathematics, College of General Studies, King Fahd University of Petroleum and Minerals, Dhahran, Saudi Arabia; Interdisciplinary Research Center for Hydrogen and Energy Storage, King Fahd University of Petroleum and Minerals, Dhahran, Saudi Arabia
Nargis Khan: Department of Mathematics, The Islamia University of Bahawalpur, Punjab, Pakistan
Siti Suzilliana Putri Mohamed Isa: Institute for Mathematical Research, Universiti Putra Malaysia, 43400 UPM Serdang, Selangor, Malaysia; Centre for Foundation Studies in Science of Universiti Putra Malaysia, Universiti Putra Malaysia, 43400 UPM Serdang, Selangor, Malaysia
Nanthini Balakrishnan: Institute for Mathematical Research, Universiti Putra Malaysia, 43400 UPM Serdang, Selangor, Malaysia
Syed M. Hussain: Department of Mathematics, Faculty of Science, Islamic University of Madinah, Madinah, 42351, Saudi Arabia

Nomenclature

B_0	uniform magnetic field
C_{fx}	skin friction
D_B	mass diffusivity coefficient
Ec	Eckert number
E_a	activation energy
K	porosity parameter
$K = 6\pi\mu r$	coefficient of drag Stokes
K^*	chemical reaction co-efficient
K^*	porous medium permeability
k^+	mean absorption coefficient
k_f	thermal conductivity of the fluid
k_r^2	reaction rate
L	reference length
M	magnetic parameter
m	fitted rate constant
Ma	Marangoni ratio parameter
Mn	Marangoni number
n	power law index parameter
Nu_x	Nusselt number
Q_0	temperature dependent source co-efficient

Q_1	temperature dependent source co-efficient
Q_e	exponential dependent heat source parameter
Q_t	temperature dependent heat source parameter
Pr	Prandtl number
q_m	mass flux
q_r	radiative heat flux
q_w	heat flux
Rc	chemical reaction rate parameter
Rd	radiation parameter
Sc	Schmidt number
Sh_x	Sherwood number
T_0	constants
We	Weissenberg number
(u, v)	velocity fields of fluid
(x, y)	Cartesian coordinates

Greek symbols

Φ_1	volume fraction of Fe_3O_4
Φ_2	volume fraction of Cu
μ_f	dynamic viscosity
T_∞	fluid ambient temperature
γ_1	thermal relaxation parameter
γ_2	concentration relaxation parameter
γ_C	surface tension coefficient for concentration
γ_T	surface tension coefficient for temperature
v_f	kinematic viscosity
ρ_f	fluid density
σ^*	Stefan–Boltzmann constant
σ_0	surface tension
σ_f	electrical conductivity
Γ	time constant
δ	elastic deformation parameter
σ	surface tension
$\psi(x, y)$	stream functions

1 Introduction

The surface tension at the two fluids' interface enables the Marangoni phenomenon to manifest in large quantities. This phenomenon was initially described in 1855. The surface tension gradient causes fluid particles to move from an area with lower surface tension to that with higher surface tension. Surface tension gradients are connected to temperature or concentration gradients. The Marangoni effect is used in a diversity of practical applications, including for convection cells, stabilization of soap films, crystal development, convection in Bénard cells, and melting of metals by an electron beam [1–12]. Of all the models of fluid with four constants, it is possible to employ the pseudoplastic fluid model to describe the shear thinning process in fluids. This phenomenon can be used in fluids that are tangent and hyperbolic. For example, soaked blood, ketchup, paint, nail polish, and whipped cream, to mention a few. Implementing the transfer of heat and the control of vertical asymmetric ducts, Nadeem and Akram [13] discussed the magnetohydrodynamic (MHD) peristaltic flow of tangent hyperbolic fluids. In the study conducted by Akbar *et al.* [14], it was identified that the same fluid flow can be modelled incorporating an extended surface. The physicochemical mechanisms of the tangent hyperbolic flow of nanoparticles in the MHD steady state conditions have been studied by Mahdy [15] while considering the effect of cylinder wall temperature variation. A study on the effect of partial slip on tangent hyperbolic fluid flow through an inclined cylinder has been conducted by Kumar *et al.* [16].

Choi [17] developed the idea of nanofluids, which are thermal conducting fluids consisting of 1–100 nm diameter nanoparticles dispersed in base fluids. Recent research has focused on mass and heat transfer in nanofluids because of their wide range of uses, including energy storage, cooling of electronic engines, solar collectors, heat exchangers, petroleum industries, photovoltaic cell thermal management, lubricants, machining technology, and drug delivery [18–31]. Figure 1 highlights the applications of nanoparticles.

Hybrid nanofluids are defined as mixtures of two dissimilar types of nanoparticles that are scattered in a base fluid. The base liquid's thermal conductivity is different from that of hybrid nanoparticles, which can be formed from two different metals or nonmetallic materials. There are numerous uses for this kind of fluid that are connected to the process of heating, and such a fluid functions effectively where a high range of temperature is required for cooling. Several fields involve the potential uses of hybrid nanofluids in the fields of refrigeration, industry, solar energy, machining and manufacturing, space, defense, *etc.* [32–35]. Figure 2 depicts applications of hybrid nanofluids.

The term "elastic deformation" describes a temporary change in a material's shape that returns to its original state when the force is removed. Few scientists have discussed about how elastic deformation affects the MHD flow of nanofluids. A stretched surface with a heat source has been used to study the impact of elastic deformation on the MHD nanofluid flow by Ahmad *et al.* [36]. The outcome of elastic deformation on the flow of Walter's-B fluid past an impermeable sheet was considered by Nandeppanavar *et al.* [37]. Khan *et al.* [38] examined the influence of elastic deformation on the flow of a viscoelastic fluid across a
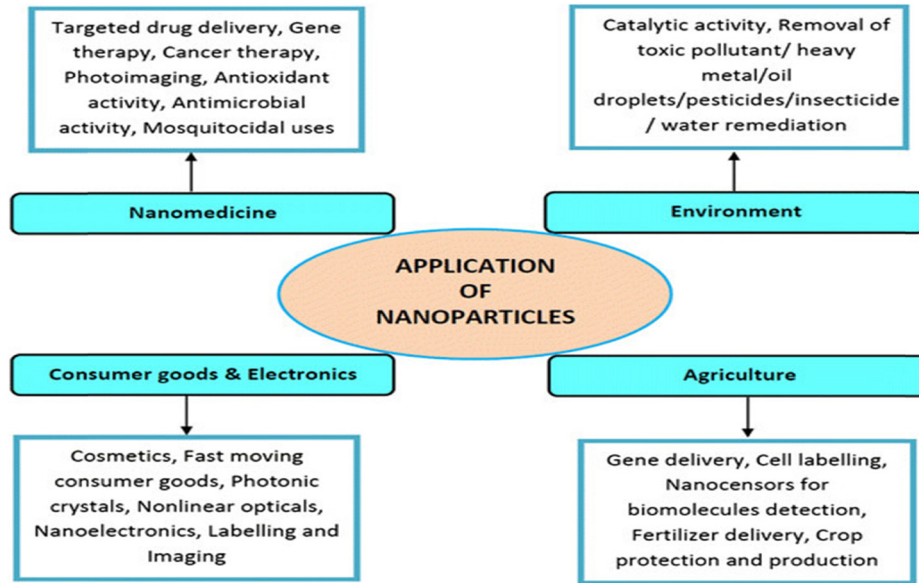
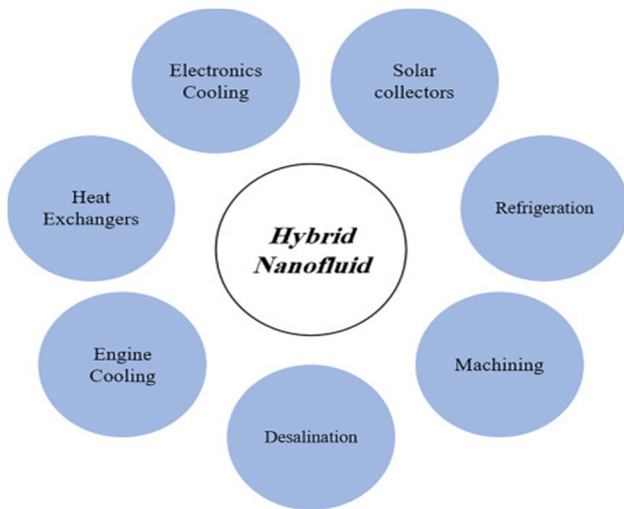**Figure 1:** Applications of nanoparticles.

**Figure 2:** Applications of hybrid nanofluids.

stretched sheet. Hakeem *et al.* [39] described how elastic deformation affected the flow of Walter's-B fluid across a sheet with a heat source. Kalaivanan *et al.* [40] numerically analyzed the outcome of elastic deformation on second grade nanofluid flow across a stretched surface.

It is well recognized that when there is a temperature differential between two things or between several sections of one object, the natural phenomenon of heat exchange takes place. Fourier's heat conduction equation has been successfully applied during the past few decades to explain the apparatus of heat transport. However, Cattaneo [41] proposed in 1948 that one might incorporate thermal relaxation time into Fourier's model to produce an efficient heat

transfer rate because different substances have various thermal relaxation times. The Cattaneo–Christov model is a time derivative model proposed by Christov [42]. Later, few scholars [43–45] used the Cattaneo–Christov model to describe the mechanisms of mass and heat transport.

To the authors' knowledge, none of the aforementioned articles have yet addressed tangent hyperbolic (Fe_3O_4 − Cu/EG) hybridized flow over a sheet with Marangoni convection. Marangoni convection finds application in a multitude of industrial, biological, and everyday circumstances, such as microfluidics, coating flow technologies, foams, and film drainage in emulsions. Therefore, this study's primary goal is to examine the Marangoni driven boundary layer flow of tangent hyperbolic hybrid nanofluids with activation energy, elastic deformation, and binary chemical reaction. The following inquiries are answered by the current study using numerical and statistical methods:

- What effects of the Marangoni ratio parameter (Ma) and Marangoni number (Mn) are seen on the solutal, velocity, and thermal profiles?
- How do the rates of mass and heat transfer change as a result of the hybrid nanofluid?
- How do thermal and solutal relaxation parameters affect thermal and solutal profiles?
- How do the volume fraction parameters of nanoparticles affect the velocity as well as temperature distribution?
- How does the thermal profile respond to the elastic deformation parameter?
- In the presence of nanofluids, what effect does the power law index, porosity, and Weissenberg number (We) parameters have on the velocity profile?
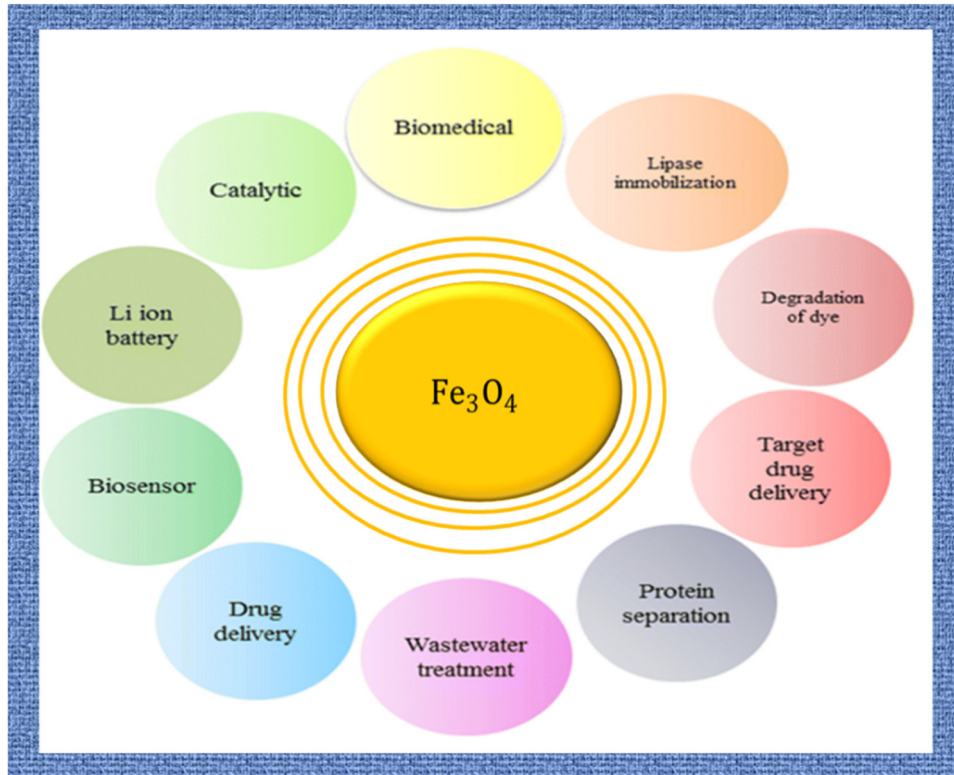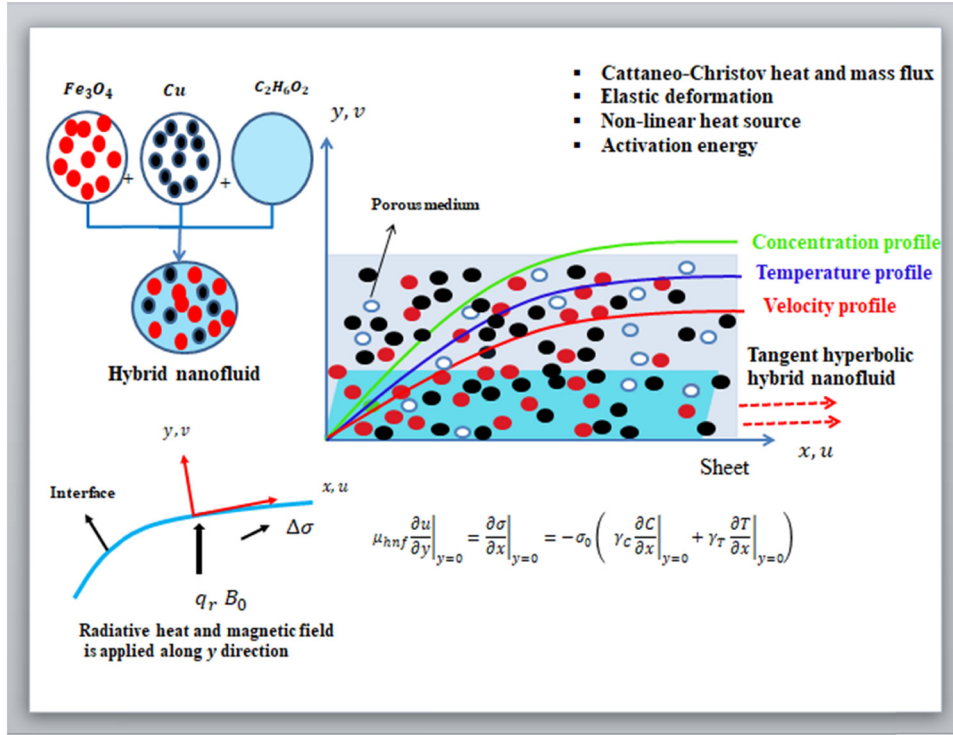
(a)
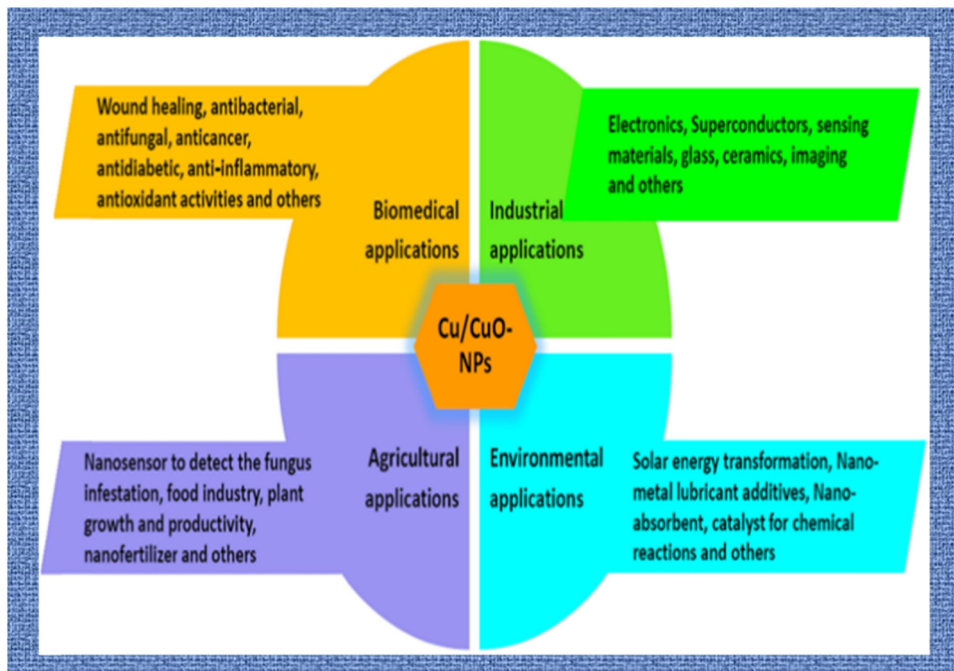
(b)

Figure 3: (a) and (b) Application of iron oxide and copper nanoparticles, respectively. (c) Flow description.

(c)

Figure 3: (*Continued*)

- How will the thermal profile be influenced by the an exponentially dependent parameter and heat source temperature?
- How does the activation energy parameter affect the concentration profile?

2 Mathematical formulation

We investigate the behavior of a surface tension-driven boundary layer flow of tangent hyperbolic hybrid nanofluids with activation energy. The characteristics of mass and heat transmission in the tangent hyperbolic hybrid nanofluid flow over plate are examined by the Cattaneo–Christov mass and heat flux model. In the proposed model, we examined the two-dimensional incompressible hybrid nanofluid

(Fe_3O_4−Cu/ethylene glycol) flowing over a surface with a magnetic field, as portrayed in Figure 3(c). In the thermal transfer examination, the functions of elastic deformation, thermal radiation, viscous dissipation and heat source are also presumed. Assume a rectangular coordinate system at $y \geq 0$. The properties of iron oxide (Fe_3O_4) and copper (Cu) nanoparticles with ethylene glycol as their base fluid are presented in Table 1. Table 2 shows theoretical representations of the nanofluid and hybrid nanofluid properties. Figure 3(a, b) display the implementations of iron oxide and Cu-nanomolecules. Surface tension varies throughout space and is affected by differences in temperature and concentration. The surface tension $\sigma = \sigma_0[1 - \gamma_T(T - T_\infty) - \gamma_C(C - C_\infty)]$ is assumed to depend on linear variation with solutal and thermal profiles.

$$\gamma_T = -\frac{1}{\sigma_0}\frac{\partial\sigma}{\partial T}\bigg|_T, \quad \gamma_C = -\frac{1}{\sigma_0}\frac{\partial\sigma}{\partial C}\bigg|_C.$$

Table 1: Nanoparticles' and base fluid's thermophysical characteristics [48,49]

Constituents	c_p (J/kgK)	k (W/mK)	σ $(\Omega m)^{-1}$	β (1/K)	ρ (kg/m^3)
Fe_3O_4	670	6	25, 000	1.3	5,200
Cu	385	401	5.96×10^7	1.67	8,933
Ethylene glycol	2,415	0.252	5.5×10^{-6}	5.7	1,114

Table 2: Thermo-physical characteristics of a hybrid nanofluid [50]

Properties	Hybrid nanofluid
Dynamic viscosity, μ_{hnf}	$A_1 = \dfrac{\mu_{hnf}}{\mu_f} = \dfrac{1}{(1 - \Phi_1)^{2.5}(1 - \Phi_2)^{2.5}}$
Density, ρ_{hnf}	$A_2 = \dfrac{\rho_{hnf}}{\rho_f} = \left[\Phi_2 \dfrac{\rho_{s_2}}{\rho_f} + (1 - \Phi_2)\left\{\Phi_1 \dfrac{\rho_{s_1}}{\rho_f} + (1 - \Phi_1)\right\}\right]$
Electrical conductivity, σ_{hnf}	$A_3 = \dfrac{\sigma_{hnf}}{\sigma_f} = \left\{1 + \dfrac{3\left[\frac{\sigma_2\Phi_2 + \sigma_1\Phi_1}{\sigma_f} - (\Phi_1 + \Phi_2)\right]}{\left[\frac{\sigma_2\Phi_2 + \sigma_1\Phi_1}{\sigma_f} + 2\right] - \left[\frac{\sigma_2\Phi_2 + \sigma_1\Phi_1}{\sigma_f} - \Phi_1\Phi_2\right]}\right\}$
Thermal conductivity, k_{hnf}	$A_4 = \dfrac{k_{hnf}}{k_{nf}} \times \dfrac{k_{nf}}{k_f} = \dfrac{(k_{s_2} + 2k_{nf}) - 2\Phi_2(k_{nf} - k_{s_2})}{(k_{s_2} + 2k_f) + \Phi_2(k_{nf} - k_{s_2})} \times \dfrac{(2k_f + k_{s_1}) - 2\Phi_1(k_f - k_{s_1})}{(2k_f + k_{s_1}) + \Phi_1(k_f - k_{s_1})}$
Heat capacitance, $(\rho c_p)_{hnf}$	$A_5 = \dfrac{(\rho c_p)_{hnf}}{(\rho c_p)_f} = \left[(1 - \Phi_2)\left\{\Phi_1 \dfrac{(\rho c_p)_{s_1}}{(\rho c_p)_f} + (1 - \Phi_1)\right\} + \Phi_2 \dfrac{(\rho c_p)_{s_2}}{(\rho c_p)_f}\right]$

According to these assumptions, the modeled equations are organized as follows [46,47]:

$$\frac{\partial u}{\partial x} + \frac{\partial v}{\partial y} = 0, \tag{1}$$

$$\rho_{hnf}\left(u\frac{\partial u}{\partial x} + v\frac{\partial u}{\partial y}\right) = \mu_{hnf}\left[(1 - n) + \sqrt{2}\,n\Gamma\frac{\partial u}{\partial y}\right]\frac{\partial^2 u}{\partial y^2}$$
$$- \frac{\mu_{hnf}}{K^*}u - \sigma_{hnf}B_0^2 u, \tag{2}$$

$$(\rho C_p)_{hnf}\left(u\frac{\partial T}{\partial x} + v\frac{\partial T}{\partial y}\right)$$
$$= k_{hnf}\left(\frac{\partial^2 T}{\partial y^2}\right) + Q_0(T - T_\infty) + Q_1 T_0 X^2 \exp\left(-n\frac{y}{L}\right) - \frac{\partial q_r}{\partial y}$$
$$+ \mu_{hnf}\left[(1 - n) + \frac{n\Gamma}{\sqrt{2}}\frac{\partial u}{\partial y}\right]\left(\frac{\partial u}{\partial y}\right)^2$$
$$- \lambda_T\left[u^2\frac{\partial^2 T}{\partial x^2} + v^2\frac{\partial^2 T}{\partial y^2} + 2uv\frac{\partial^2 T}{\partial x\partial y}\right.$$
$$+ \left(u\frac{\partial u}{\partial x} + v\frac{\partial u}{\partial y}\right)\frac{\partial T}{\partial x} + \left(u\frac{\partial v}{\partial x} + v\frac{\partial v}{\partial y}\right)\frac{\partial T}{\partial y}$$
$$- \delta k_0\left[\frac{\partial u}{\partial y}\frac{\partial}{\partial y}\left(u\frac{\partial u}{\partial x} + v\frac{\partial u}{\partial y}\right)\right], \tag{3}$$

$$u\frac{\partial C}{\partial x} + v\frac{\partial C}{\partial y}$$
$$= D_B\frac{\partial^2 C}{\partial y^2} - k_r^2(C - C_\infty)\left(\frac{T}{T_\infty}\right)^m \exp\left(-\frac{E_a}{k^* T}\right)$$
$$- \lambda_C\left[u^2\frac{\partial^2 C}{\partial x^2} + v^2\frac{\partial^2 C}{\partial y^2} + 2uv\frac{\partial^2 C}{\partial x\partial y}\right.$$
$$+ \left(u\frac{\partial u}{\partial x} + v\frac{\partial u}{\partial y}\right)\frac{\partial C}{\partial x} + \left(u\frac{\partial v}{\partial x} + v\frac{\partial v}{\partial y}\right)\frac{\partial C}{\partial y}. \tag{4}$$

The relative boundary constraints are listed as follows [44]:

$$\mu_{hnf}\frac{\partial u}{\partial y} = \frac{\partial \sigma}{\partial x} = -\sigma_0\left(\gamma_T\frac{\partial T}{\partial x} + \gamma_C\frac{\partial C}{\partial x}\right), \quad v = 0, \tag{5}$$
$$T = T_\infty + T_0 X^2, \text{ at } y = 0,$$

$$C = C_\infty + C_0 X^2, \text{ at } y = 0,$$
$$u \to 0, \quad T \to T_\infty, \quad C \to C_\infty, \text{ at } y \to \infty.$$

The proposed coordinates are taken in the following form:

$$\psi = v_f X f(\eta), \eta = \frac{y}{L}, \quad X = \frac{x}{L}, T = T_\infty + T_0 X^2 \theta(\eta), \tag{6}$$

$$u = \frac{\partial \psi}{\partial y}, \quad v = -\frac{\partial \psi}{\partial x}, \quad C = C_\infty + C_0 X^2 \phi(\eta).$$

These are mathematical equations in reduced nondimensional forms.

$$A_1 f'''(\eta)((1 - n) + n\text{We}f''(\eta)) + A_2(f''(\eta)f(\eta)$$
$$- [f'(\eta)]^2) - A_3 M f'(\eta) - A_1 K f'(\eta) = 0, \tag{7}$$

$$A_4\theta''(\eta) + \text{Rd}\theta''(\eta) + Q_t\theta(\eta) + Q_t \exp(-n\eta)$$
$$+ A_5\text{Pr}\left(\begin{array}{c} f(\eta)\theta'(\eta) \\ -2f'(\eta)\theta(\eta) \end{array}\right) + \text{PrEc}A_1((1 - n)$$
$$+ n\text{We}f''(\eta))(f''(\eta))^2 \tag{8}$$
$$- \text{Pr}\gamma_1\left(\begin{array}{c} 4f'^2(\eta)\theta(\eta) - f(\eta)f''(\eta)\theta(\eta) \\ -3f(\eta)f'(\eta)\theta'(\eta) + f^2(\eta)\theta''(\eta) \end{array}\right)$$
$$- \delta K_1\text{Ec}(f'(\eta)(f''(\eta))^2 - f(\eta)f''(\eta)f'''(\eta)) = 0,$$

$$\phi''(\eta) + \text{Sc}(f(\eta)\phi'(\eta) - 2f'(\eta)\phi(\eta))$$

$$- \text{Sc}\gamma_2 \begin{pmatrix} 4f'^2(\eta)\phi(\eta) - f(\eta)f''(\eta)\phi(\eta) \\ - 3f(\eta)f'(\eta)\phi'(\eta) + f^2(\eta)\phi''(\eta) \end{pmatrix} - \text{ScRc}(1 \qquad (9)$$

$$+ \delta\theta(\eta))^m \exp\left(\frac{-E}{1 + \delta\theta(\eta)}\right)\phi(\eta) = 0.$$

The boundary conditions that have been transformed are as follows:

$$f''(0) = -\frac{2\text{Mn}(1 + \text{Ma})}{A_1}, \quad f(0) = 0, \theta(0) = 1, \phi(0) = 1, \qquad (10)$$

$$f'(\infty) \to 0, \theta(\infty) \to 0, \phi(\infty) \to 0,$$

where $\text{We} = \frac{\Gamma X v_f}{L^2}$ is the Weissenberg number, $K = \frac{L^2}{K^*}$ is the porosity parameter, $\text{Pr} = \frac{v_f(\rho C_p)_f}{k_f}$ is the Prandtl number, $M = \frac{\sigma_1 B_0^2 L^2}{\mu_f}$ is the magnetic parameter, $\text{Sc} = \frac{v_f}{D_f}$ is the Schmidt number, $E = \frac{E_a}{k^* T_\infty}$ is the non-dimensional activation energy, $\text{Ec} = \frac{(v_f)^2}{L^2 C_p}$ is the Eckert number, $Q_t = \frac{Q_0 L^2}{(\rho C_p)_f v_f}$ is the temperature dependent heat source parameter, $\text{Rc} = \frac{k_r^2 L^2}{v_f}$ is the chemical reaction rate parameter, $Q_e = \frac{Q_1 L^2}{(\rho C_p)_f v_f}$ is the exponential dependent heat source parameter, $\gamma_1 = \frac{v_f \lambda_T}{L^2}$ is the thermal relaxation parameter, $\delta^* = \frac{T_0 X^2}{T_\infty}$ is the temperature difference, $\text{Ma} = \frac{C_0 \gamma_C}{T_0 \gamma_T}$ is the Marangoni ratio parameter, $\text{Mn} = \frac{\sigma_0 T_0 \gamma_T X L}{X \mu_f v_f}$ is the Marangoni number, $\text{Rd} = \frac{16\sigma^{**} T_\infty^3}{3k^* k_f}$ is the radiation parameter, $\gamma_2 = \frac{v_f \lambda_C}{L^2}$ is the solutal relaxation parameter, and $K_1 = \frac{K_0}{v_f L^2}$ is the elastic deformation parameter.

3 Physical quantities of engineering interest

The rate of mass and heat transmission at the surface is often measured as follows:

$$C_{\text{fx}} = \frac{\tau_w}{\rho}, \quad \text{Nu}_x = \frac{xq_w}{k_f(T_w - T_\infty)},$$
$$\text{Sh}_x = \frac{xq_m}{D_B(C_w - C_\infty)}, \qquad (11)$$

$$\tau_w = \mu_{\text{hnf}}\left[(1 - n)\frac{\partial u}{\partial y} + \frac{n\Gamma}{\sqrt{2}}\left(\frac{\partial u}{\partial y}\right)^2\right], \qquad (12)$$

$$q_w = -\left[k_{\text{hnf}} + \frac{16T_\infty^3 \sigma^*}{3k^*}\right]\frac{\partial T}{\partial y}\bigg|_{y=0}, \qquad (13)$$

$$q_m = -D_m\frac{\partial C}{\partial y}\bigg|_{y=0}. \qquad (14)$$

Here, q_w describes the heat flux, τ_w denotes the skin friction, and q_m shows the mass flux.

$$C_{\text{fx}} = A_1\left((1 - n)f''(0) + \frac{1}{2}n\text{We}(f''(0))^2\right), \qquad (15)$$

$$\text{Nu}_x(\text{Re}_x)^{-0.5} = -(A_4 + \text{Rd})\theta'(0), \qquad (16)$$

$$\text{Sh}_x(\text{Re}_x)^{-0.5} = -\phi'(0). \qquad (17)$$

4 Numerical method: Runge–Kutta–Fehlberg-45th (RKF-45) method

There does not seem to be a precise solution for the current model, which is highly non-linear. The RKF-45 approach's high-level language and interactive environment are used to solve these equations numerically. Using the replacements, the ordinary differential equations (ODEs) (9)–(11) become the first-order ODEs (Eq. (19)).

$$f = y_1, \quad f' = y_2, \quad f'' = y_3, \quad f''' = y_3', \theta = y_4, \quad \theta' = y_5,$$
$$\theta'' = y_5', \phi = y_6, \phi' = y_7, \phi'' = y_7'$$

in the following:

$$y_1' = y_2, \quad y_2' = y_3,$$
$$y_3' = \frac{1}{((1 - n) + n\text{We}y_3)A_1}(A_2(y_2^2 - y_1 y_3) + MA_3 y_2 \quad (18)$$
$$+ A_1 K y_2,$$

$$y_4' = y_5,$$
$$y_5' = (A_4 + \text{Rd} - \text{Pr}\gamma_1(y_1)^2)^{-1}(A_5(\text{Pr}(2y_2 y_4 - y_1 y_5)$$
$$- \text{PrEc}A_1((1 - n) + n\text{We}y_3)(y_3)^2 \qquad (19)$$
$$+ \text{Pr}\gamma_1(4(y_2)^2 y_4 - y_1 y_3 y_4 - 3y_1 y_2 y_5) - \text{Pr}Q_t y_4$$
$$- \text{Pr}Q_e \exp(-n\eta) + \delta K_1 \text{Ec}(y_2(y_3)^2 - y_1 y_3 y_3')),$$

$$y_6' = y_7,$$
$$y_8' = \left[1 - \text{Sc}\gamma_2(y_1)^2)^{-1}\text{Sc}\left[2y_2 y_7 - y_1 y_8\right]\right.$$
$$+ \text{ScRc}(1 + \delta^* y_4)^m \exp\left(\frac{-E}{1 + \delta^* y_4}\right)y_6 \qquad (20)$$
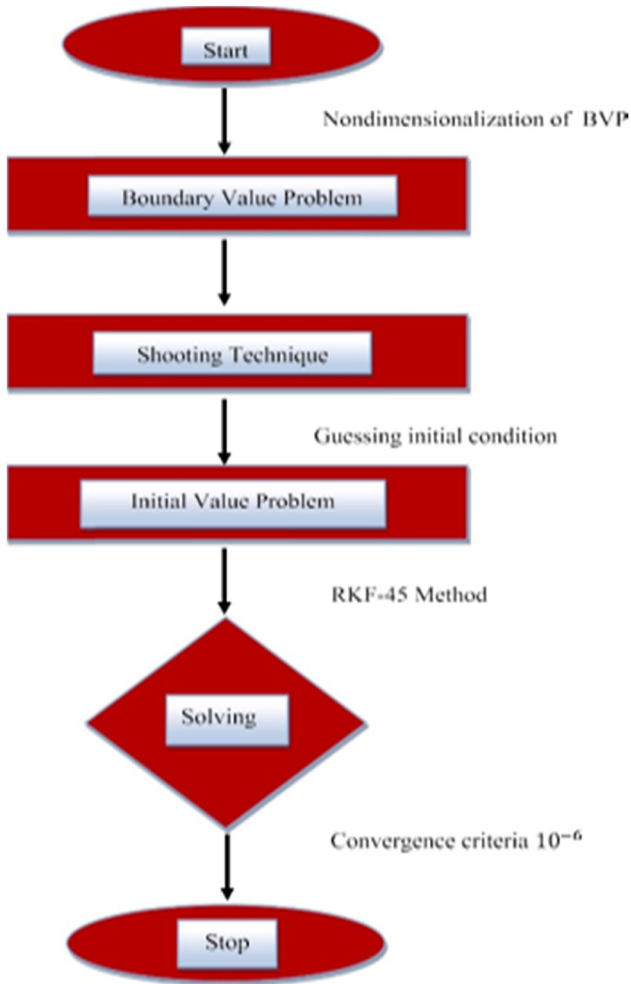$$+ \text{Sc}\gamma_2(4(y_2)^2 y_6 - y_1 y_3 y_6 - 3y_1 y_2 y_7)\bigg].$$

Figure 4: Flow chart.

Boundary conditions:

$$y_1(0) = 0, \qquad y_2(0) = m_1,$$

$$y_3(0) = -2\frac{Mn(1 + Ma)}{A_1}, \quad y_4(0) = 1, y_5(0) = m_2, \tag{21}$$

$$y_6(0) = 1, \quad y_7(0) = m_3. \tag{22}$$

The simulation procedure is portrayed in Figure 4.

5 Results and discussion

The shooting method is effective in transforming BVPs into IVPs. The main emphasis is on evaluating dimensionless quantities, including $f'(\eta), \theta(\eta)$, and $\phi(\eta)$ profiles of thermal, velocity, and concentration, respectively, for numerous values of parameters, *e.g.,* Ma, We, n, K, M, Rd, $\gamma_1, \gamma_2, \delta$, Mn, Rc, E, Φ_1, and Φ_2. The influences of n and We on $f'(\eta)$ are shown in Figure 5(a) and (b). The fluid velocity is additionally slowed down as we increase We, as noted in Figure 5(a). In fact, the We is directly related to the relaxation time; higher values of We increase the relaxation time and provide more resistance to fluid motion, which affects the velocity of hybrid nanofluids and nanofluids. The fluids that are described by the power law index can be characterized by pseudoplastic fluids ($n < 1$) or dilatant fluids ($n > 1$). According to the values of n for the shear thinning phenomena, Figure 5(b) shows a reduction in the velocity profile of hybrid nanofluids and nanofluids. This is because
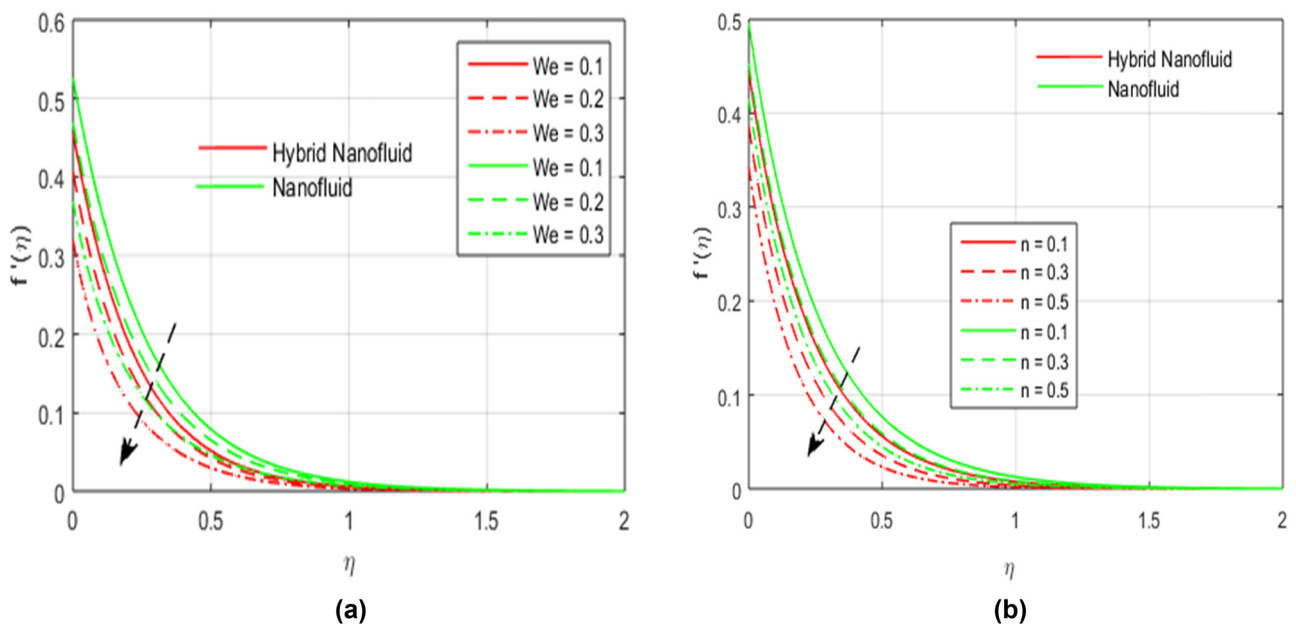

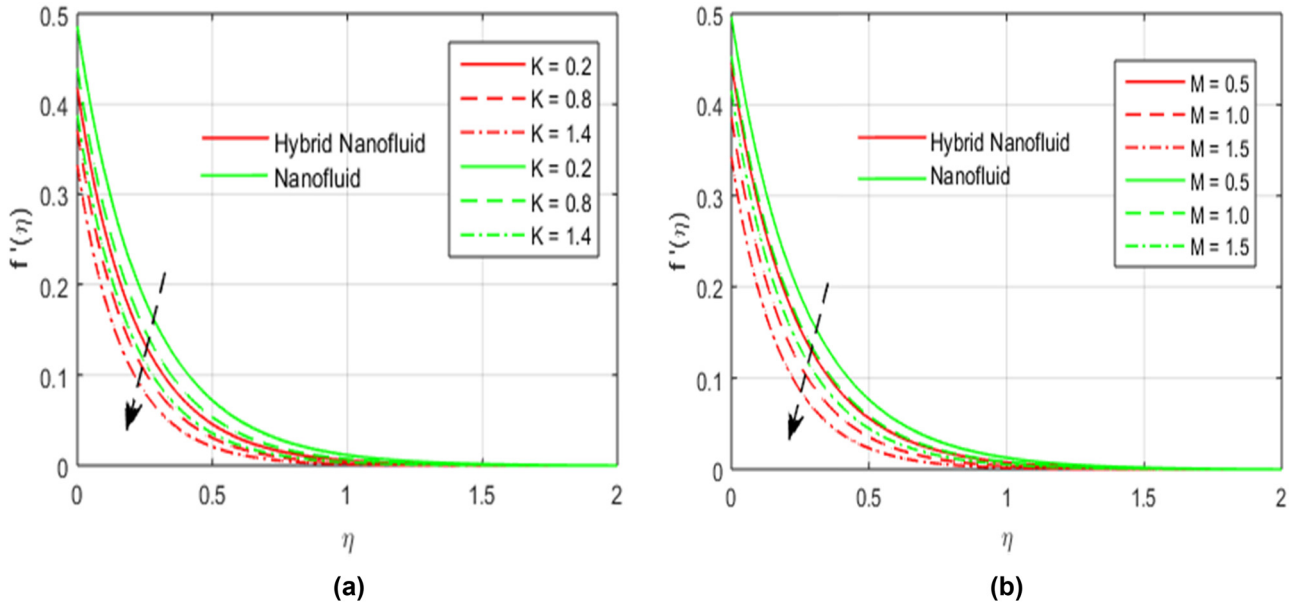**Figure 5:** (a) and (b) Effect of We and n on $f'(\eta)$.

Figure 6: (a) and (b) Effect of K and M on $f'(\eta)$.

a rising power law index corresponds to a rise in viscosity, which causes a decrease in fluid velocity. The outcome of K on $f'(\eta)$ is shown in Figure 6(a). The figure clearly shows that the velocity profile of hybrid nanofluids and nanofluids falls as K is increased. This is due to the fact that a porous medium's widening pores provide resistive forces that work against flow and lower velocity profiles. The outcome of an M on $f'(\eta)$ is shown in Figure 6(b). Statistics clearly show

that the velocity profile depreciates as M augments. This is brought about by the Lorentz force, which opposes the flow and arises as M is increased.

The MHD force enhances the thermal boundary layer and reduces the momentum boundary layer. The outcome of nanoparticle volume fraction of Fe_3O_4 and Cu nanoparticles Φ_1 and Φ_2 on $f'(\eta)$ and $\theta(\eta)$ is shown in Figures 7(a) and (b), 8(a) and (b); as we increase Φ_1 and Φ_2, this causes
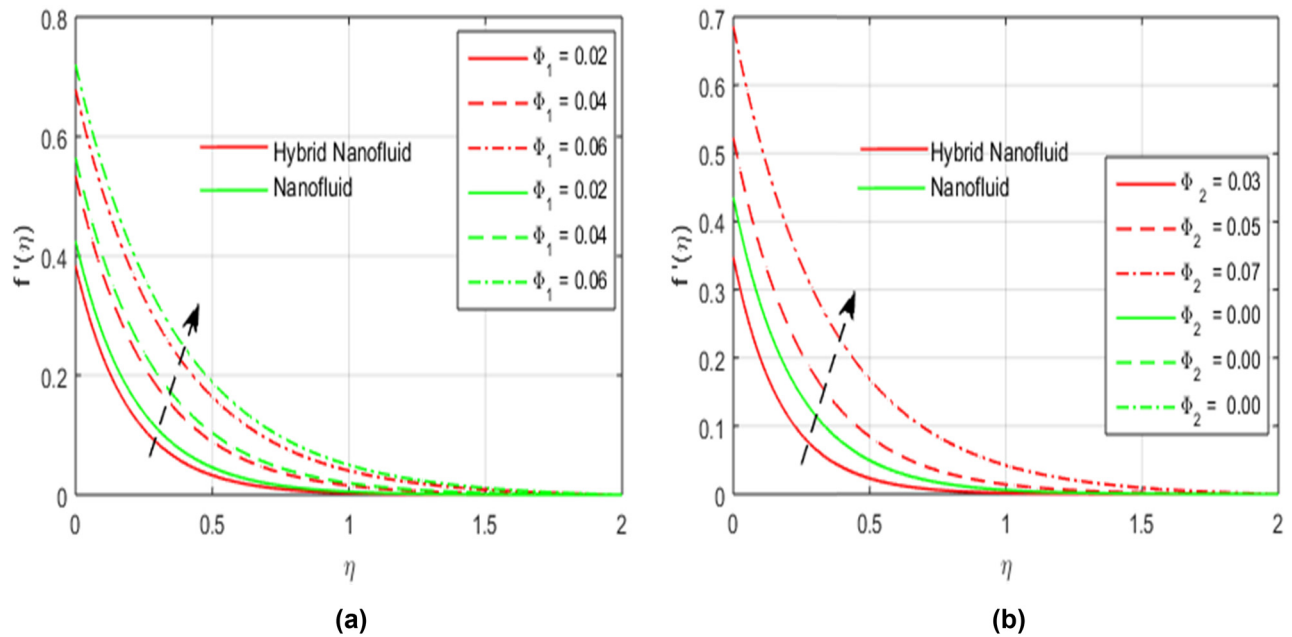

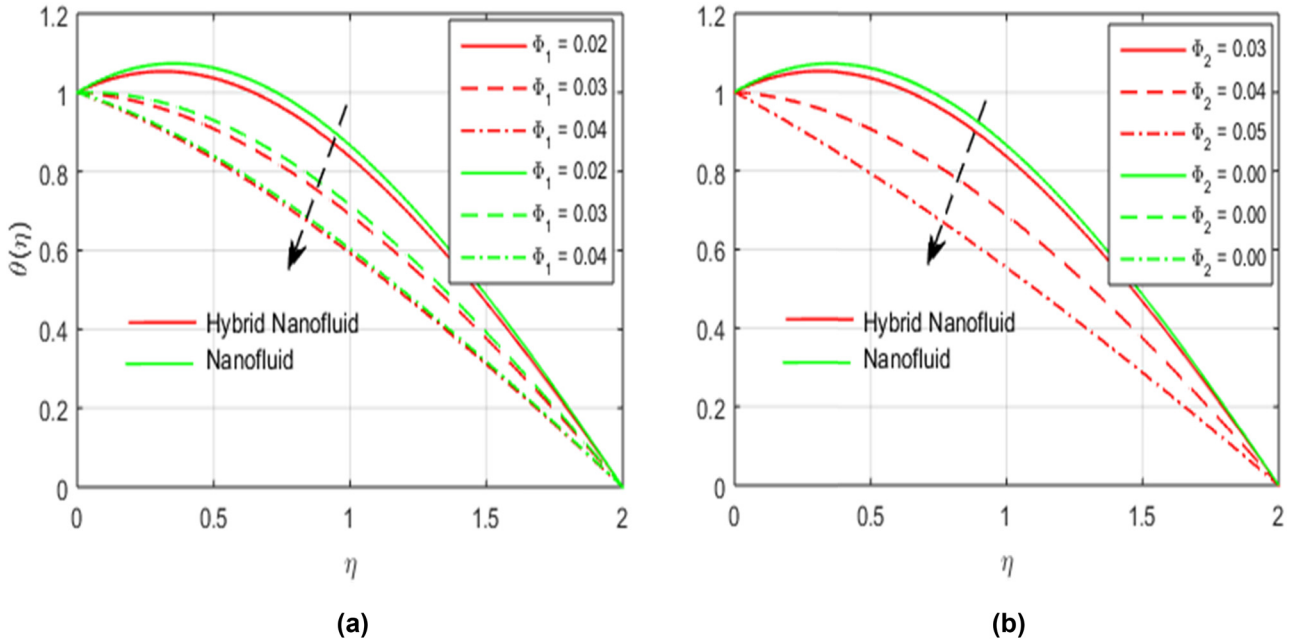**Figure 7:** (a) and (b) Effect of Φ_1 and Φ_2 on $f'(\eta)$.

Figure 8: (a) and (b) Effect of Φ_1 and Φ_2 on $\theta(\eta)$.

an improvement in the velocity profile and declines the thermal profile of hybrid nanofluids and nanofluids. The responses of $\theta(\eta)$ against an increase in Rd are shown in Figure 9(a). The thermal radiation phenomena serve as energy sources for the fluid system; it is anticipated that $\theta(\eta)$ increases when the thermal radiation parameter (Rd) is increased. The influence of δ on $\theta(\eta)$ is shown in Figure 9(b). It is noticed that the $\theta(\eta)$ profile reduces with higher values of δ, the elastic deformation parameter. The influence of Q_t and Q_e on $\theta(\eta)$ is shown in Figure 10(a) and (b). It is clear that when heat generation is increased, the temperature profiles improve. When Q_t and Q_e are positive, the
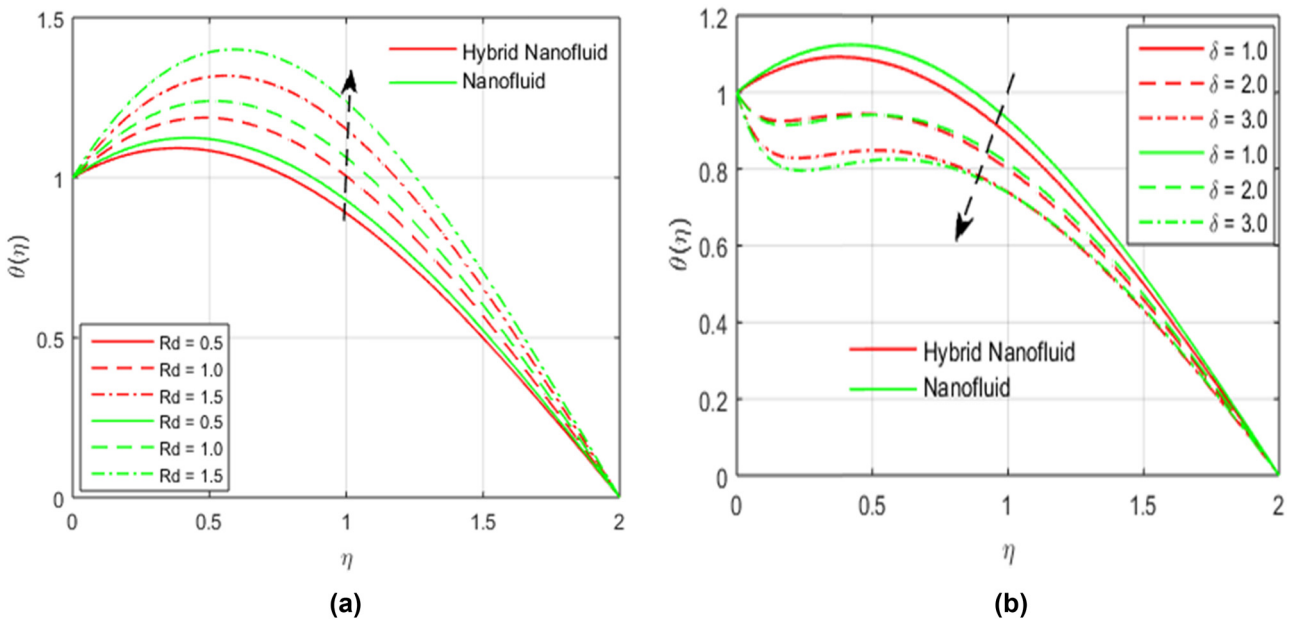

Figure 9: (a) and (b) Effect of Rd and δ on $\theta(\eta)$.
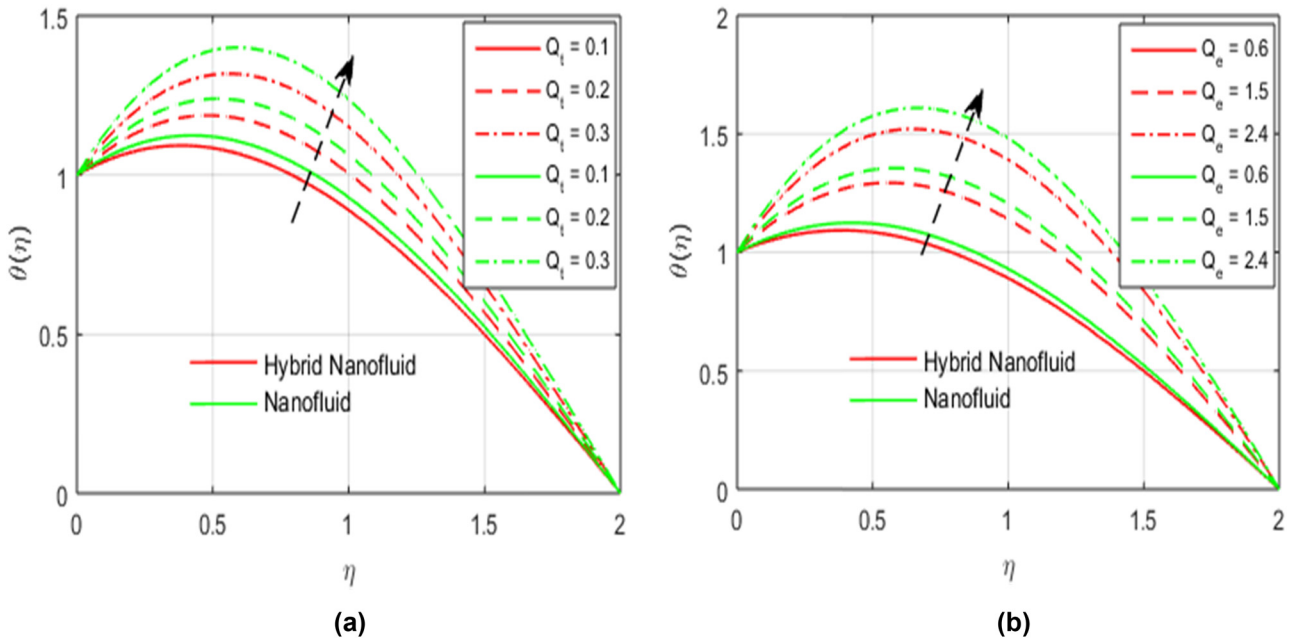
Figure 10: (a) and (b) Effect of Q_t and Q_e on $\theta(\eta)$.

heat source factor shows how much heat is generated and is dispersed across the environment. It is demonstrated that energy generated by the boundary thermal layer causes the fluid's temperature to rise for increasing values of Q_t and $Q_e > 0$.

The impacts of γ_1 and γ_2 on $\theta(\eta)$ and $\phi(\eta)$ are described in Figure 11(a) and (b). They adequately show that $\theta(\eta)$ and $\phi(\eta)$ profiles as well as the associated concentration and

thermal boundary layer thicknesses tend to decline with increasing relaxation times. Additionally, it is clear from these figures that, in contrast to the Cattaneo–Christov model, where mass and heat instantly diffuse throughout the medium, the thermal and solutal boundary layer thicknesses are larger for the traditional Fick's law and Fourier's law (i.e., $\gamma_1 = \gamma_2 = 0$). Figure 12(a) and (b) depicts the outcome of E and Rc on the concentration profile. Here, an
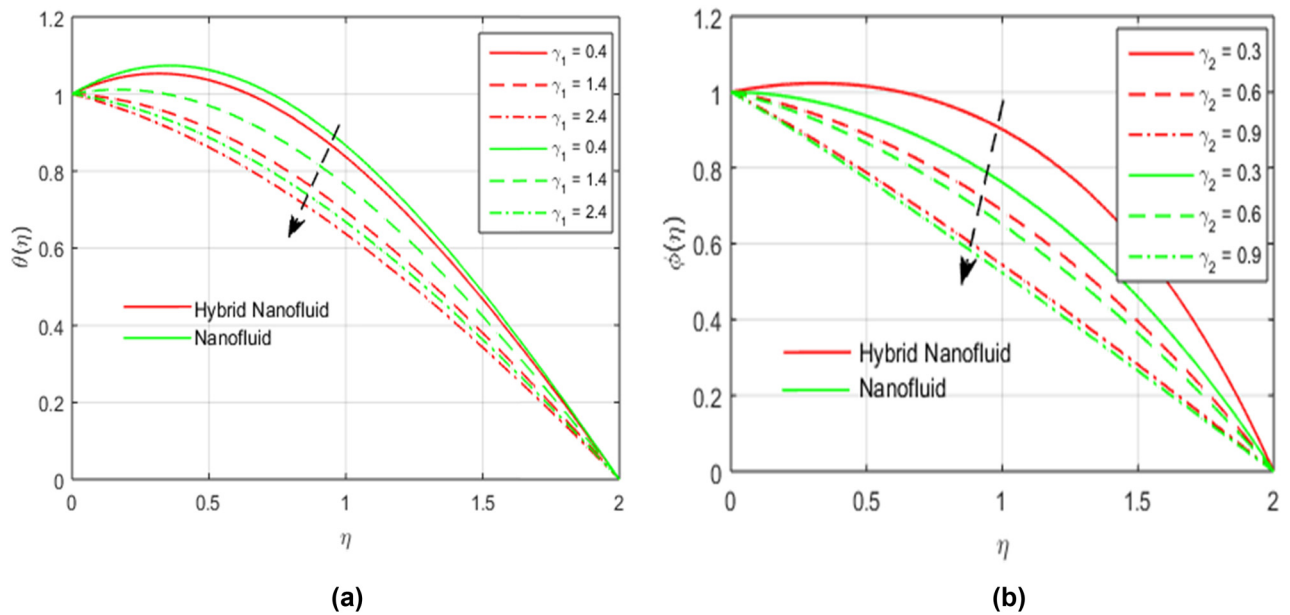
Figure 11: (a) and (b) Effect of γ_1 and γ_2 on $\theta(\eta)$.
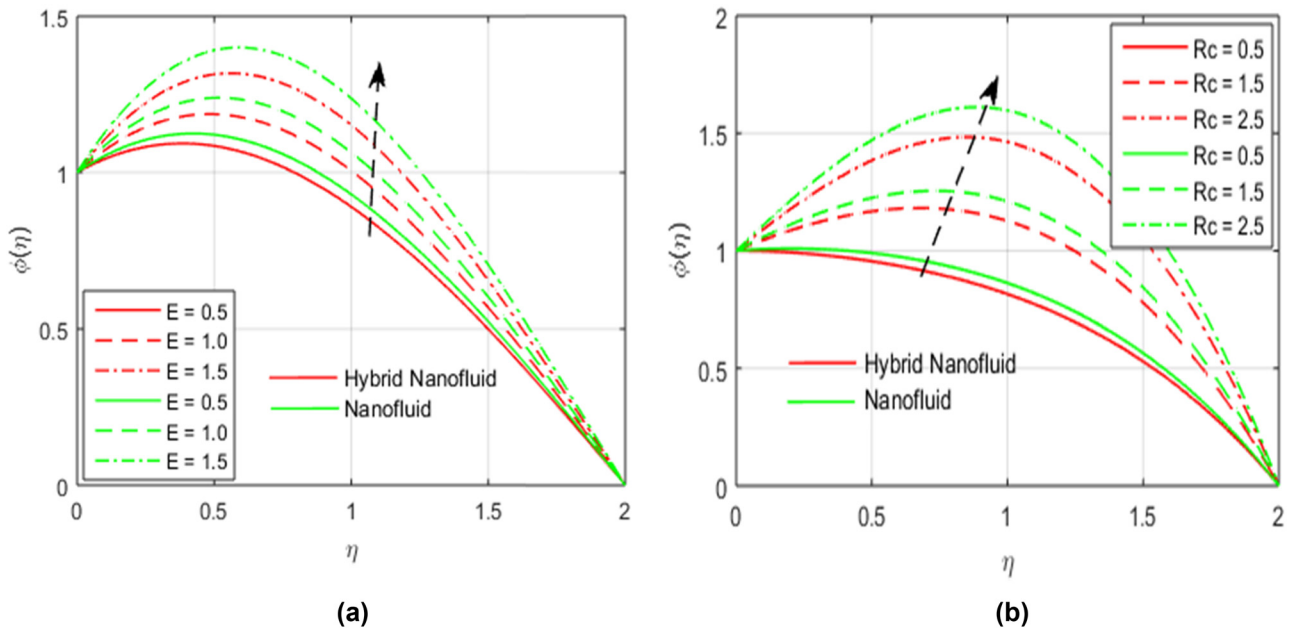
Figure 12: (a) and (b) Effect of E and Rc on $\phi(\eta)$.

increase in E and Rc enhances $\phi(\eta)$. Each system that receives activation energy experiences a drop in acceleration and heat, which leads to a low reaction rate constant, according to the Arrhenius equation. The chemical reaction causes a rise in particle concentration. As the activation energy E rises, the Arrhenius mechanism declines. The generative chemical reaction is ultimately initiated by this, increasing the nanoparticles' concentration profile.

The outcomes of Mn number and Ma on $f'(\eta)$, $\theta(\eta)$, and $\phi(\eta)$ profiles of the tangent hyperbolic hybrid nanofluid are depicted in Figures 13(a) and (b), 14(a) and (b). The graph illustrates how the increase in the value of Mn and Ma augments the velocity $f'(\eta)$ and concentration $\phi(\eta)$ profiles of the hybrid nanofluid and nanofluid. These phenomena relate to the variation of the surface of a given material. For liquid streams, the thermosolutal Marangoni

Figure 13: (a) and (b) Effect of Mn and Ma on $\theta(\eta)$.
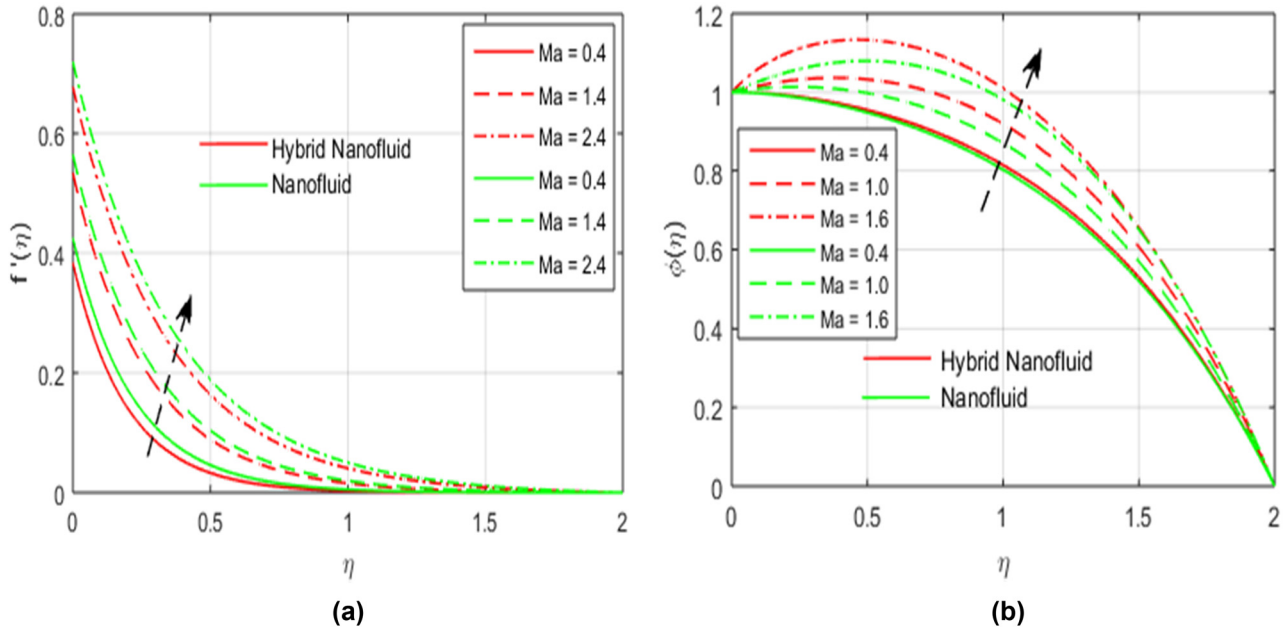
Figure 14: (a) and (b) Effect of Ma on $f'(\eta)$ and $\phi(\eta)$.

Table 3: Outcome of numerous parameters on skin friction

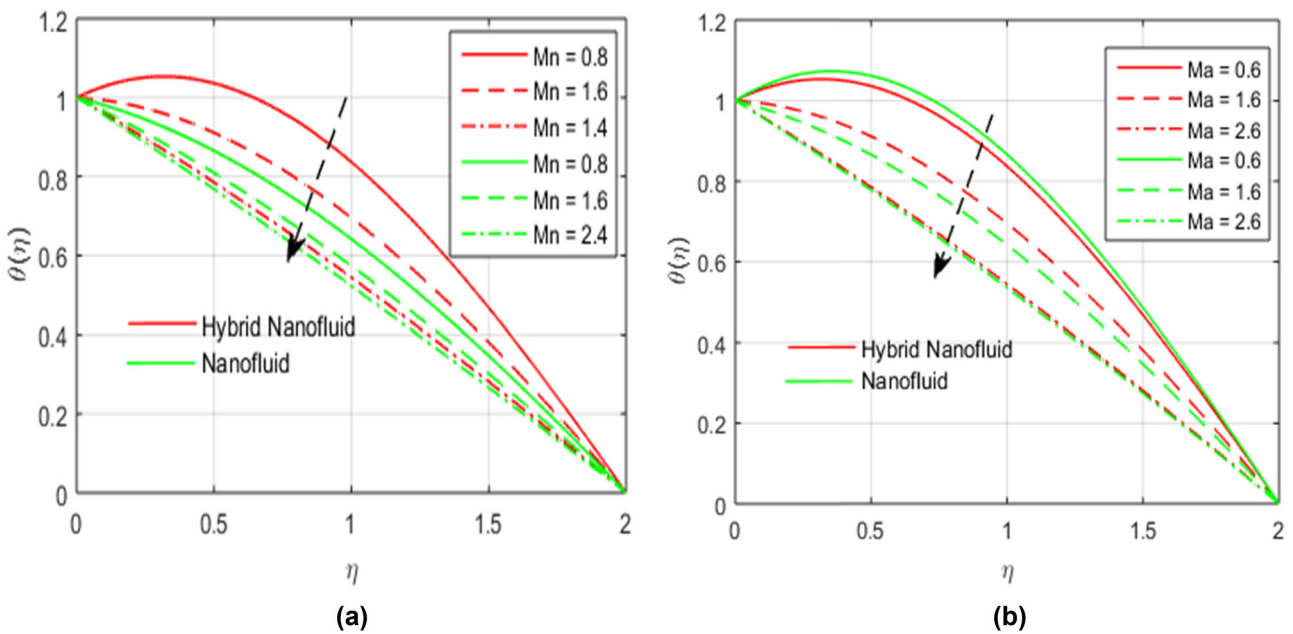| | | | | | | | $C_{fx} = A_1((1{-}n)f''(0) + \frac{1}{2}nWe(f''(0))^2)$ | |
| | | | | | | | Hybrid nanofluid | Nanofluid |
Ma	We	n	K	M	Φ_1	Φ_2	$Fe_3O_4 + Cu{-}C_2H_6O_2$	$Fe_3O_4{-}C_2H_6O_2$
0.2	0.3	0.4	0.1	0.6	0.05	0.04	2.450192	2.126052
0.3							2.450297	2.126100
0.4							2.450327	2.126287
	0.3						2.450199	2.126052
0.4	**0.4**	0.3	0.1	0.6	0.05	0.04	2.637727	2.313587
	0.5						2.825247	2.501110
		0.2					2.971968	2.555241
0.1	2.0	**0.3**	0.1	0.6	0.05	0.04	2.241128	2.009590
		0.4					2.010678	1.964382
			0.2				2.450199	2.126052
0.2	2.0	0.3	**0.3**	0.6	0.05	0.04	2.637709	2.313556
			0.4				2.825220	2.501062
				0.2			2.450199	2.126052
0.2	2.0	0.3	0.1	**0.3**	0.05	0.04	2.637665	2.313555
				0.4			2.825145	2.501060
					0.02		2.450199	2.126052
0.2	2.0	0.3	0.1	0.6	**0.04**	0.04	3.756961	3.245493
					0.06		7.515934	6.465740
						0.01	2.450199	…………
						0.03	2.710004	…………
0.2	2.0	0.3	0.1	0.6	0.05	**0.05**	3.496819	…………

Bold values are showing the variation of the current model.

Table 4: Change in the Nu_x

									$Nu_x = -(Re)^{1/2}[A_4 + Rd]\theta'(0)$	
									Hybrid nanofluid	Nanofluid
Ma	Q_t	Q_e	Ec	γ_1	Rd	Φ_1	Φ_2	δ	$Fe_3O_4 + Cu-C_2H_6O_2$	$Fe_3O_4-C_2H_6O_2$
0.2	0.3	0.4	0.1	0.6	0.7	0.03	0.04	0.4	5.372312	5.082330
0.3									5.434445	5.082545
0.4									5.472839	5.083362
	0.3								5.372312	5.082330
0.4	**0.4**	0.3	0.1	0.6	0.7	0.03	0.04	0.4	5.472013	5.182040
	0.5								6.772014	6.280130
		0.2							5.846152	5.082330
0.1	2.0	**0.3**	0.1	0.6	0.7	0.03	0.04	0.4	5.848545	5.085030
		0.4							5.849315	5.088430
			0.2						5.033365	5.082142
0.2	2.0	0.3	**0.3**	0.6	0.7	0.03	0.04	0.4	5.372184	5.082330
			0.4						5.392286	5.082342
				0.2					5.033783	4.925243
0.2	2.0	0.3	0.1	**0.3**	0.7	0.03	0.04	0.4	5.034058	4.925441
				0.4					5.034110	4.925807
					0.2				5.372184	5.082142
0.2	2.0	0.3	0.1	0.6	**0.3**	0.03	0.04	0.4	6.741922	6.452015
					0.4				8.111659	7.821888
						0.02			5.372312	5.082330
0.2	2.0	0.3	0.1	0.6	0.7	**0.04**	0.04	0.4	6.244517	5.814387
						0.06			7.872433	7.181170
							0.01		5.372312	………….
0.2	2.0	0.3	0.1	0.6	0.7	0.03	**0.02**	0.4	5.587332	………….
							0.03		11.813890	………….
								0.2	4.221601	4.144061
0.2	2.0	0.3	0.1	0.6	0.7	0.03	0.04	**0.4**	5.439877	5.315836
								0.6	6.658171	6.487623

Bold values are showing the variation of the current model.

effect works as a pouring force; therefore, a higher Marangoni effect will always cause a more knotted velocity profile. This graph proves that as the value of Ma increases, the temperature profile is lowered by a considerable amount. The thermosolutal Mn is directly correlated with the surface tension. The bulk attraction of the liquid to the particles in the surface layer produces surface tension, a physical characteristic of liquid surfaces. As an outcome, the thermal profile decreases as the surface tension rises, enhancing the attraction between molecules on the surface. As a result, the temperature gradient is reduced (Tables 3–5).

6 Final remarks

In this investigation, we examined the flow of a tangent hyperbolic hybrid nanofluid across a surface with a permeable material and elastic deformation. The explanations of the concentration, thermal and velocity fields are shown for a variety of flow parameters. Following are the key findings of the current investigation:

- The velocity and concentration profiles are improved, and the heat transfer is declined, when the Ma increases.
- The thermal and concentration gradients are declined when the concentration and thermal relaxation parameter are augmented.
- The thermal profile is declined and the velocity gradient is increased as the nanoparticle concentration enhances.
- The heat transmission is improved by increasing the values of heat source and heat Rd.
- The thermal gradient declines as the elastic deformation parameter increases.
- A rise in the activation energy tends to elevate the concentration.
- The Nu_x, skin friction factor, and Sh_x are increased when the Ma is increased.

Table 5: Influence of several parameters on Sh_x

							$Sh_x = -(Re)^{1/2}\,\phi'(0)$	
							Hybrid nanofluid $Fe_3O_4 + Cu-C_2H_6O_2$	Nanofluid $Fe_3O_4-C_2H_6O_2$
Ma	**Rc**	**Sc**	$\boldsymbol{\gamma_2}$	**E**	$\boldsymbol{\Phi_1}$	$\boldsymbol{\Phi_2}$		
0.1	0.3	0.4	0.1	0.6	0.05	0.04	1.370334	1.370771
0.3							1.370602	1.371268
0.5							1.371030	1.371865
	0.3						1.370349	1.370629
0.2	**0.6**	0.3	0.1	0.6	0.05	0.04	1.370249	1.370529
	0.9						1.370144	1.370492
			0.2				1.371226	1.370870
0.2	2.0	**0.3**	0.1	0.6	0.05	0.04	1.271200	1.350848
		0.4					1.160249	1.260827
			0.1				1.370249	1.370629
0.2	2.0	0.3	**0.3**	0.6	0.05	0.04	1.375249	1.470820
			0.4				2.740302	1.570629
				0.2			2.398473	2.298177
0.2	2.0	0.3	0.1	**0.4**	0.05	0.04	1.370634	1.282461
				0.6			1.370438	1.200207
					0.02		1.370888	1.370771
0.2	2.0	0.3	0.1	0.6	**0.04**	0.04	2.740855	1.370644
					0.06		2.740989	1.371022
						0.01	1.370334	…………..
						0.03	1.370205	…………..
0.2	2.0	0.3	0.1	0.6	0.05	**0.05**	1.369677	…………..

Bold values are showing the variation of the current model.

- An augmentation in the volume fraction of hybrid nano-particles improves the friction factor, Nu_x, and Sh_x of tangent hyperbolic hybrid nanofluids and nanofluids.

Author contributions: All authors have accepted responsibility for the entire content of this manuscript and approved its submission.

Conflict of interest: The authors state no conflict of interest.

Data availability statement: The datasets generated and/or analyzed during the current study are available from the corresponding author on reasonable request.

References

[1] Abbas M, Khan N, Shazad SA. Thermophoretic particle depositionin Carreau-Yasuda fluid over chemical reactive Riga plate with Marangoni convection. Adv Mech Eng. 2023;15(1):1–14.

[2] Abbas M, Khan N, Hashmi MS, Younis J. Numerically analysis of Marangoni convective flow of hybrid nanofluid over an infinite disk with thermophoresis particle deposition. Sci Rep. 2023;13(1):5036.

[3] Zhuang YJ, Zhu QY. Numerical study on combined buoyancy–Marangoni convection heat and mass transfer of power-law nanofluids in a cubic cavity filled with a heterogeneous porous medium. Int J Heat Mass Transf. 2018;71:39–54.

[4] Wang TS, Shi WY. Influence of substrate temperature on Marangoni convection instabilities in a sessile droplet evaporating at constant contact line mode. Int J Heat Mass Transf. 2019;131:1270–8.

[5] Kumar G, Gireesha K, Prasannakumara BJ, Makinde OD. Impact of chemical reaction on marangoni boundary layer flow of a Casson nano liquid in the presence of uniform heat source sink. Diffus Found. 2017;11:22–32.

[6] Chu YM, Khaled KA, Khan N, Khan MI, Khan SU, Hashmi MS, et al. Study of Buongiorno's nanofluid model for flow due to stretching disks in presence of gyrotactic microorganisms. Ain Shams Eng J. 2021;12(4):3975–85.

[7] Khan N, Riaz I, Hashmi MS, Musmar SA, Khan SU, Abdelmalek Z, et al. Aspects of chemical entropy generation in flow of Casson nanofluid between radiative stretching disks. Entropy. 2020;22:495.

[8] Khan N, Mahmood T, Hashmi MS. Oham solution for thin film flow of third-grade fluid through porous medium over an inclined plane. Heat Transf. 2013;44:719–31.

[9] Khan N, Mahmood T. The influence of slip condition on the thin film flow of a third order fluid. Int J Nonlinear Sci. 2012;13:105–16.

[10] Tamanna MN, Ferdows M, Lorenzini G, Shamshuddin MD, Usman M. Numerical investigation of heat transfer enhancement on tangent hyperbolic fluid over a stretching sheet with an inclined magnetic field filled with hybrid nanofluids. J Engin Thermophys. 2024;33:55–72. doi: 10.1134/S1810232824010065.

[11] Salawu SO, Akinola EI, Shamshuddin MD. Entropy generation and current density of tangent hyperbolic Cu-C2H6O2 and ZrO2-Cu/C2H6O2 hybridized electromagnetic nanofluid: A thermal power application. South Afr J Chem Eng. 2023;46:1–11. doi: 10.1016/j.sajce.2023.07.003.

[12] Shamshuddin MD, Saeed A, Asogwa KK, Usman, Jamshed W. A semi-analytical approach to investigate the entropy generation in a tangent hyperbolic magnetized hybrid nanofluid flow upon a stretchable rotating disk. J Magnetism Magnetic Mater. 2023;574:170664. doi: 10.1016/j.jmmm.2023.170664.

[13] Nadeem S, Akram S. Magnetohydrodynamic peristaltic flow of a hyperbolic tangent fluid in a vertical asymmetric channel with heat transfer. Acta Mech Sin. 2011;27:237–50.

[14] Akbar NS, Nadeem S, Haq RU, Khan ZH. Numerical solution of magnetohydrodynamic boundary layer flow of tangent hyperbolic fluid towards a stretching sheet. Indian J Phys. 2013;87:1121–4.

[15] Mahdy A. Entropy generation of tangent hyperbolic nanofluid flow past a stretched permeable cylinder: variable wall temperature. Proc Inst Mech Eng Part E: J Process Mech Engin. 2019;233:570–80.

[16] Kumar YVKR, Kumar PV, Bathul S. Effect of slip on peristaltic pumping of a hyperbolic tangent fluid in an inclined asymmetric channel. Adv Appl Sci Res. 2014;5:91–108.

[17] Choi SUS, (ed.). Enhancing thermal conductivity of fluids with nanoparticles. Vol. 231, San Francisco, CA: ASME Publications-Fed; 1995. p. 99–106.

[18] Mahanthesh B, Gireesha JB, Gorla RR, Abbasi FM, Shehzad SA. Numerical solutions for magnetohydrodynamic flow of nanofluid over a bidirectional non-linear stretching surface with prescribed surface heat flux boundary. J Magn Magn Mater. 2016;417:189–96.

[19] Prasannakumara BC, Gireesha BJ, Gorla RSR, Krishnamurthy MR. Effects of chemical reaction and nonlinear thermal radiation on Williamson nanofluid slip flow over a stretching sheet embedded in a porous medium. J Aerosp Eng. 2016;29:04016019.

[20] Sheikholeslami M, Shehzad SA. Magnetohydrodynamic nanofluid convection in a porous enclosure considering heat flux boundary condition. Int J Heat Mass Transf. 2017;106:1261–9.

[21] Majeed AH, Bilal S, Mahmood R, Malik MY. Heat transfer analysis of viscous fluid flow between two coaxially rotated disks embedded in permeable media by capitalizing non-Fourier heat flux model. Phys A: Stat Mech Appl. 2020;540:123182. doi: 10.1016/j.physa.2019.123182.

[22] Majeed AH, Mahmood R, Liu D, Ali MR, Hendy AS, Zhao B, et al. Flow and heat transfer analysis over a pair of heated bluff bodies in a channel: Characteristics of non-linear rheological models. Case Stud Therm Eng. 2024;53:103827. doi: 10.1016/j.csite.2023.103827.

[23] Majeed AH, Irshad S, Ali B, Hussein AK, Shah NA, Botmart T. Numerical investigations of nonlinear Maxwell fluid flow in the presence of non-Fourier heat flux theory: Keller box-based simulations. AIMS Math. 2023;8(5):12559–75. doi: 10.3934/math.2023631.

[24] Majeed AH, Mahmood R, Hamadneh NN, Siddique I, Khan I, Alshammari N. Periodic flow of non-Newtonian fluid over a uniformly heated block with thermal plates: A Hybrid Mesh-Based Study. Front Phys. 2022;10:829085. doi: 10.3389/fphy.2022.829085.

[25] Ahmad S, Ali K, Kottakkaran NS, Faridi AA, Khan N, Jamshed W, et al. Features of Cu and TiO2 in the flow of engine oil subject to thermal jump conditions. Sci Rep. 2021;11(10):1038.

[26] Kottakkaran NS, Faridi AA, Ahmad S, Khan N, Ali K, Jamshed W, et al. Cumulative impact of micropolar fluid and porosity on MHD channel flow: a numerical study. Coatings. 2022;12(10):3390.

[27] Khan N, Hashmi MS, Khan SU, Chaudhry F, Tlili I, Iskander, et al. Effects of homogeneous and heterogeneous chemical features on oldroyd-B fluid flow between stretching disks with velocity and temperature boundary assumptions. Math Probl Eng. 2020;10:5284906.

[28] Khan N, Riaz M, Hashmi MS, Khan SU, Tlili I, Mubbashar N. Soret and Dufour features in peristaltic motion of chemically reactive fluid in a tapered asymmetric channel in the presence of Hall current. J Phys Commun. 2020;4(10):1088.

[29] Si X, Li H, Zheng L, Shen Y, Zhang X. A mixed convection flow and heat transfer of pseudo-plastic power law nanofluids past a stretching vertical plate. Int J Heat Mass Transf. 2017;105:350–8.

[30] Hayat T, Sajjad R, Alsaedi A, Muhammad T, Ellahi R. On squeezed flow of couple stress nanofluid between two parallel plates. Results Phys. 2017;7:553–61.

[31] Kumar R, Shilpa S, Sheikholeslami M, Shehzad SA. Nonlinear thermal radiation and cubic autocatalysis chemical reaction effects on the flow of stretched nanofluid under rotational oscillations. J Colloid Interface Sci. 2017;505:253–65.

[32] Majeed AH, Mahmood R, Shahzad H, Pasha AA, Islam N, Rahman MM. Numerical simulation of thermal flows and entropy generation of magnetized hybrid nanomaterials filled in a hexagonal cavity. Case Stud Therm Eng. 2022;39:102293. doi: 10.1016/j.csite.2022.102293.

[33] Yuan H, Jan AZ, Majeed AH, Shi L, Kędzia K, Ferrás LJ, et al. Characteristics of synovial trihybrid nanofluid activation energy and Marangoni convective flow: A Computational framework of local thermal non-equilibrium. Case Stud Therm Eng. 2024;59:104519. doi: 10.1016/j.csite.2024.104519.

[34] Majeed AH, Jan AZ, Alamri AM, AlQahtani SA, Ali MR, Hendy AS. Recent developments in the Darcy-Forchheimer model of magnetized tetra hybrid nanofluid activation energy/joule heating in a stenotic artery. Case Stud Therm Eng. 2024;59:104346. doi: 10.1016/j.csite.2024.104346.

[35] Majeed AH, Siddique I, Mehmood A, Ghazwani HA, Manzoor S, Ahmad S. Finite element simulations of Herschel–Bulkley visco-plastic materials over a cylinder: Drag and lift correlation analysis. Mod Phys Lett B. 2024;38:2450248. doi: 10.1142/S0217984924502488.

[36] Ahmad B, Iqbal Z, Maraj E, Ijaz S. Utilization of elastic deformation on Cu–Ag nanoscale particles mixed in hydrogen oxide with unique features of heat generation/absorption: Closed form outcomes. Arabian J Sci Eng (Springer Science & Business Media BV). 2018;44(6):5949–60.

[37] Nandeppanavar MM, Subhas MA, Jagadish T. Heat transfer in a Walter's liquid B fluid over an impermeable stretching sheet with non-uniform heat source/sink and elastic deformation. Commun Nonlinear Sci Numer Simulat. 2010;15:1791–802.

[38] Khan SK, Subhas AM, Ravi MS. Visco-elastic MHD flow, heat and mass transfer over a porous stretching sheet with dissipation of energy and stress work. Heat Mass Transf. 2003;40:47–57.

[39] Hakeem AKA, Vishnu Ganesh N, Ganga B. Effect of heat radiation in a Walter's liquid B fluid over a stretching sheet with non-uniform heat source/sink and elastic deformation. J King Saud Univ – Eng Sci. 2014;26(2):168–75.

[40] Kalaivanan R, Ganga B, Vishnu Ganesh N, Abdul Hakeem AK. Effect of elastic deformation on nano-second grade fluid flow over a stretching surface. Front Heat Mass Transf. 2018;10:20–9.

[41] Cattaneo C. Sulla conduzione del calore, Atti Semin. Mat Fis Univ Modena Reggio Emilia. 1948;3:83–101.

[42] Christov CI. On frame indifferent formulation of the Maxwell-Cattaneo model of finite-speed heat conduction. Mech Res Commun. 2009;36:481–6.

[43] Khan MH. On Cattaneo–Christov heat flux model for Carreau fluid flow over a slendering sheet. Results Phys. 2017;7:310–9.

[44] Hayat T, Khan MI, Waqas M, Alsaedi A. On Cattaneo–Christov heat flux in the flow of variable thermal conductivity Eyring–Powell fluid. Results Phys. 2017;7:446–50.

[45] Ali ME, Sandeep N. Cattaneo-Christov model for radiative heat transfer of magnetohydrodynamic Casson-ferrofluid: a numerical study. Results Phys. 2017;7:21–30.

[46] Mahdy A, Hoshoudy GA. Two-phase mixed convection nanofluid flow of a dusty tangent hyperbolic past a nonlinearly stretching sheet. J Egypt Math Soc. 2019;27:44.

[47] Rasool G, Zhang T, Shafiq A. Marangoni effect in second grade forced convective flow of water based nanofluid. J Adv Nanotechnol. 2018;1:50–61.

[48] Ahmad S, Ali K, Faridi AA, Ashraf M. Novel thermal aspects of hybrid nanoparticles Cu-TiO2 in the flow of ethylene glycol. Int Commun Heat Mass Transf. 2021;129:105708.

[49] Ahmad S, Ali K, Ashraf M, Khalifa HA, Aziz ElSeabee FA, Tag El Din ES. Analysis of pure nanofluid (GO/engine oil) and hybrid nanofluid (GO–Fe_3O_4/engine oil): Novel thermal and magnetic features. Nanotechnol Rev. 2022;11:2903–15. doi: 10.1515/ntrev-2022-0486.

[50] Li S, Leng Y, Atta G, Ahmad S, Ali K, Idris SA, et al., Thermal attributes of sodium alginate (Na.C6H7O6) based binary and ternary hybrid nanofluids under activation energy and induced magnetic field environment. Case Stud Therm Eng. 2024;59:104449. doi: 10.1016/j.csite.2024.104449.